Front. Phys. 13(5), 135102 (2018)
https://doi.org/10.1007/s11467-018-0777-z

RESEARCH ARTICLE

Discrete Boltzmann model for implosion- and explosion-related compressible flow with spherical symmetry

Ai-Guo Xu[1,2,†], Guang-Cai Zhang[1], Yu-Dong Zhang[1,3], Pei Wang[1], Yang-Jun Ying[1]

[1] *National Key Laboratory of Computational Physics, Institute of Applied Physics and Computational Mathematics, P.O. Box 8009-26, Beijing 100088, China*

[2] *Center for Applied Physics and Technology, MOE Key Center for High Energy Density Physics Simulations, College of Engineering, Peking University, Beijing 100871, China*

[3] *Key Laboratory of Transient Physics, Nanjing University of Science and Technology, Nanjing 210094, China*

Corresponding author. E-mail: †Xu_Aiguo@iapcm.ac.cn

Received December 13, 2017; accepted March 9, 2018

To kinetically model implosion- and explosion-related phenomena, we present a theoretical framework for constructing a discrete Boltzmann model (DBM) with spherical symmetry in spherical coordinates. To achieve this goal, a key technique is to use *local* Cartesian coordinates to describe the particle velocity in the kinetic model. Therefore, geometric effects, such as divergence and convergence, are described as a "force term". To better access the nonequilibrium behavior, even though the corresponding hydrodynamic model is one-dimensional, the DBM uses a discrete velocity model (DVM) with three dimensions. A new scheme is introduced so that the DBM can use the same DVM regardless of whether or not there are extra degrees of freedom. As an example, a DVM with 26 velocities is formulated to construct the DBM at the Navier–Stokes level. Via the DBM, one can study simultaneously the hydrodynamic and thermodynamic nonequilibrium behaviors in implosion and explosion processes that are not very close to the spherical center. The extension of the current model to a multiple-relaxation-time version is straightforward.

Keywords discrete Boltzmann model, compressible flows, spherical symmetry, geometric effects, thermodynamic nonequilibrium

PACS numbers 51.10.+y, 47.11.-j

1 Introduction

Compressible flows are ubiquitous in natural and engineering fields. The study of compressible flow is often associated with the flight of modern high-speed aircraft and atmospheric reentry of space-exploration vehicles, high-Mach-number combustion systems [1], hydrodynamic instabilities in inertial confinement fusion [2], materials under strong shock or detonation [3], etc. Common flows that are generally of large scale and slow kinetic mode can be described by the Navier–Stokes equations. It has been known that the Navier–Stokes model encounters problems in describing shock waves, detonation waves, boundary layers, microflows, and flows with very quick kinetic modes. The physical reasons can be understood as follows: According to the Chapman–Enskog analysis, the Navier–Stokes equations are the set of hydrodynamic equations where only the first-order thermodynamic nonequilibrium (TNE) in the Knudsen number is taken into account. However, the Knudsen numbers in those small structures and quick kinetic modes are not very small, which challenges the validity of Navier–Stokes modeling. At the same time, in traditional Navier–Stokes modelling, the TNE effects are coarsely described by the viscous stress and heat flux with phenomenological constitutive relations.

In recent years, a variety of kinetic models based on the Boltzmann equation have been proposed to simulate nonequilibrium flows [4–23]. The discrete Boltzmann method (DBM) [24–37] recently developed from the lattice Boltzmann method (LBM) [38–52] belongs to this category. The Boltzmann equation presents values and evolutions of all kinetic moments of the distribution func-

*arXiv: 1803.03117.

Frontiers of Physics

tion. Similar to, but different from, the original Boltzmann equation, the DBM presents not only values and evolutions of conserved kinetic moments (density, momentum, and energy) but also those of some nonconserved kinetic moments. The former correspond to those described by hydrodynamic equations; the latter complement the former in providing a finer description of specific status and can help to understand the nonlinear constitutive relations of nonequilibrium flows [24, 25]. In recent years, the DBM has brought some new physical insights into the fundamental mechanisms of various complex flow systems. For example, the TNE intensity has been used to discriminate the spinodal decomposition stage and the domain growth stage in phase separation [28]; the abundant TNE characteristics have been used to distinguish and capture various interfaces [26, 29] in numerical experiments and to investigate the fundamental mechanisms for entropy increase [31] in complex flows. Some of the new observations brought by the DBM, for example, the nonequilibrium fine structures of shock waves, have been confirmed and supplemented by the results of molecular dynamics [53–55].

Up to now, most DBM models for compressible fluids are in Cartesian coordinates, except for one in polar coordinates [26]. In traditional modeling of implosion and explosion processes, a one-dimensional hydrodynamic model is frequently used to describe system with spherical symmetry and a system with cylindrical symmetry with translational symmetry. In this work we aim to construct a DBM for compressible flow systems with spherical symmetry.

This paper is organized as follows: In Section 2 we briefly review the kinetic and hydrodynamic models of the fluid system. In terms of their correlations, we formulate two sets of measures for the deviation of the system from its thermodynamic equilibrium. The discrete Boltzmann models are formulated and some numerical calculation results are shown in Section 3. Section 4 presents the discussion and conclusion.

2 Fluid models

2.1 Kinetic model

The Boltzmann BGK model reads

$$\partial_t f + \boldsymbol{v}\cdot\nabla f = -\frac{1}{\tau}(f - f^{eq}), \tag{1}$$

where $f = f(\boldsymbol{R},\boldsymbol{v},t) = f(x,y,z,v_x,v_y,v_z,t)$, $\boldsymbol{R} = x\hat{\boldsymbol{x}} + y\hat{\boldsymbol{y}} + z\hat{\boldsymbol{z}}$, and $\boldsymbol{v} = v_x\hat{\boldsymbol{x}} + v_y\hat{\boldsymbol{y}} + v_z\hat{\boldsymbol{z}}$ in Cartesian coordinates.

In spherical coordinates, as shown in Fig. 1, the position $\boldsymbol{R} = r\hat{\boldsymbol{r}}$. The three parameters r, θ, and φ are the radial, azimuth, and zenith angle, respectively. The

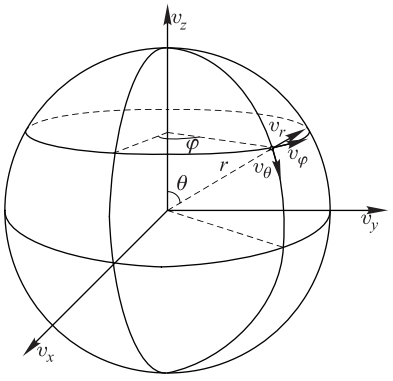

Fig. 1 Diagrammatic drawing of spherical coordinate frame and Cartesian coordinate frame.

unit vectors, $\hat{\boldsymbol{r}}$, $\hat{\boldsymbol{\theta}}$, and $\hat{\boldsymbol{\varphi}}$, are the changing directions of the position vector $\boldsymbol{R}$ along the three parameters, r, θ, and φ, respectively, i.e., $\mathrm{d}\boldsymbol{R} = \hat{\boldsymbol{r}}\mathrm{d}r + r\hat{\boldsymbol{\theta}}\mathrm{d}\theta + r\sin\theta\hat{\boldsymbol{\varphi}}\mathrm{d}\varphi$. Obviously, $\hat{\boldsymbol{r}}$, $\hat{\boldsymbol{\theta}}$, and $\hat{\boldsymbol{\varphi}}$ are orthogonal to each other and satisfy the following relationships: $\hat{\boldsymbol{\varphi}} = \hat{\boldsymbol{r}}\times\hat{\boldsymbol{\theta}}$, $\hat{\boldsymbol{\theta}} = \hat{\boldsymbol{\varphi}}\times\hat{\boldsymbol{r}}$, $\hat{\boldsymbol{r}} = \hat{\boldsymbol{\theta}}\times\hat{\boldsymbol{\varphi}}$. It is easy to find that

$$\begin{aligned}
\mathrm{d}\hat{\boldsymbol{r}} &= (\hat{\boldsymbol{\varphi}}\mathrm{d}\theta + \hat{\boldsymbol{z}}\mathrm{d}\varphi)\times\hat{\boldsymbol{r}} = \hat{\boldsymbol{\theta}}\mathrm{d}\theta + \hat{\boldsymbol{\varphi}}\sin\theta\mathrm{d}\varphi,\\
\mathrm{d}\hat{\boldsymbol{\theta}} &= (\hat{\boldsymbol{\varphi}}\mathrm{d}\theta + \hat{\boldsymbol{z}}\mathrm{d}\varphi)\times\hat{\boldsymbol{\theta}} = -\hat{\boldsymbol{r}}\mathrm{d}\theta + \hat{\boldsymbol{\varphi}}\cos\theta\mathrm{d}\varphi,\\
\mathrm{d}\hat{\boldsymbol{\varphi}} &= (\hat{\boldsymbol{\varphi}}\mathrm{d}\theta + \hat{\boldsymbol{z}}\mathrm{d}\varphi)\times\hat{\boldsymbol{\varphi}} = -(\hat{\boldsymbol{r}}\sin\theta + \hat{\boldsymbol{\theta}}\cos\theta)\mathrm{d}\varphi.
\end{aligned}$$

The particle velocity $\boldsymbol{v}$ can use either of the two sets of Cartesian coordinates, $(\hat{\boldsymbol{x}},\hat{\boldsymbol{y}},\hat{\boldsymbol{z}})$ or $(\hat{\boldsymbol{r}},\hat{\boldsymbol{\theta}},\hat{\boldsymbol{\varphi}})$, as follows: $\boldsymbol{v} = v_x\hat{\boldsymbol{x}} + v_y\hat{\boldsymbol{y}} + v_z\hat{\boldsymbol{z}}$ or $\boldsymbol{v} = v_r\hat{\boldsymbol{r}} + v_\theta\hat{\boldsymbol{\theta}} + v_\varphi\hat{\boldsymbol{\varphi}}$, where $v_r = \boldsymbol{v}\cdot\hat{\boldsymbol{r}}$, $v_\theta = \boldsymbol{v}\cdot\hat{\boldsymbol{\theta}}$, and $v_\varphi = \boldsymbol{v}\cdot\hat{\boldsymbol{\varphi}}$ are the projections of $\boldsymbol{v}$ in the $\hat{\boldsymbol{r}}$, $\hat{\boldsymbol{\theta}}$, and $\hat{\boldsymbol{\varphi}}$ directions, respectively. Correspondingly, the distribution function f can also be described in two different forms,

$$f = f(r,\theta,\varphi,v_x,v_y,v_z,t) \tag{2}$$

or

$$f = f(r,\theta,\varphi,v_r,v_\theta,v_\varphi,t). \tag{3}$$

In this work we will use the latter form, Eq. (3). Under definition (3), it should be stressed that, when we calculate the spatial derivative, ∇f, even though the particle velocity $\boldsymbol{v}$ is fixed, its three components vary with the position $\boldsymbol{R}$, i.e., $v_r = v_r(\boldsymbol{R})$, $v_\theta = v_\theta(\boldsymbol{R})$, and $v_\varphi = v_\varphi(\boldsymbol{R})$. We use the symbol "$\nabla|_{\boldsymbol{v}}$" to replace "$\nabla$" in Eq. (1) to stress that $\boldsymbol{v}$ is fixed when calculating the spatial derivatives. Thus, Eq. (1) can be rewritten as

$$\partial_t f + \boldsymbol{v}\cdot\nabla|_{\boldsymbol{v}} f = -\frac{1}{\tau}(f - f^{eq}). \tag{4}$$

According to definition (3),

$$\nabla|_{\boldsymbol{v}} f = \nabla|_{v_r,v_\theta,v_\varphi} f + \nabla v_r\frac{\partial f}{\partial v_r} + \nabla v_\theta\frac{\partial f}{\partial v_\theta} + \nabla v_\varphi\frac{\partial f}{\partial v_\varphi}, \tag{5}$$

where

$$\nabla v_r = \frac{v_\theta}{r}\hat{\boldsymbol{\theta}} + \frac{v_\varphi}{r}\hat{\boldsymbol{\varphi}}, \tag{6}$$

$$\nabla v_\theta = -\frac{v_r}{r}\hat{\boldsymbol{\theta}} + \frac{v_\varphi \cos\theta}{r\sin\theta}\hat{\boldsymbol{\varphi}}, \tag{7}$$

$$\nabla v_\varphi = -\left(\frac{v_r}{r} + \frac{v_\theta \cos\theta}{r\sin\theta}\right)\hat{\boldsymbol{\varphi}}. \tag{8}$$

Substituting Eqs. (5)–(8) into Eq. (4) gives the Boltzmann equation in spherical coordinates,

$$\partial_t f + \boldsymbol{v}\cdot\nabla|_{v_r,v_\theta,v_\varphi} f + \frac{v_\theta^2 + v_\varphi^2}{r}\frac{\partial f}{\partial v_r} + \left(\frac{v_\varphi^2\cos\theta}{r\sin\theta} - \frac{v_r v_\theta}{r}\right)\frac{\partial f}{\partial v_\theta} - \left(\frac{v_r v_\varphi}{r} + \frac{v_\varphi v_\theta\cos\theta}{r\sin\theta}\right)\frac{\partial f}{\partial v_\varphi} = -\frac{1}{\tau}(f - f^{eq}). \tag{9}$$

For a macroscopic system with spherical symmetry, the distribution function f does not depend on the angles θ and φ, i.e.,

$$f = f(r, v_r, v_\theta, v_\varphi, t), \tag{10}$$

and f is invariant under the rotation in the subspace of (v_θ, v_φ), i.e.,

$$f(r, v_r, v_\theta, v_\varphi, t) = f(r, v_r, v'_\theta, v'_\varphi, t) \tag{11}$$

when

$$v_\theta^2 + v_\varphi^2 = v_\theta'^2 + v_\varphi'^2. \tag{12}$$

Now, we take $v'_\theta = v_\theta + \mathrm{d}v_\theta$ and $v'_\phi = v_\phi + \mathrm{d}v_\phi$. From Eq. (11) we can get

$$f(r, v_r, v'_\theta, v'_\varphi, t) = f(r, v_r, v_\theta, v_\varphi, t) + \frac{\partial f}{\partial v_\theta}\mathrm{d}v_\theta + \frac{\partial f}{\partial v_\phi}\mathrm{d}v_\phi, \tag{13}$$

which gives

$$\frac{\partial f}{\partial v_\theta}\mathrm{d}v_\theta + \frac{\partial f}{\partial v_\phi}\mathrm{d}v_\phi = 0. \tag{14}$$

From Eq. (12) we can get

$$\frac{\mathrm{d}v_\theta}{v_\phi} = -\frac{\mathrm{d}v_\phi}{v_\theta}. \tag{15}$$

Therefore,

$$v_\theta\frac{\partial f}{\partial v_\varphi} - v_\varphi\frac{\partial f}{\partial v_\theta} = 0. \tag{16}$$

Using the conditions (10) and (16) in Eq. (9) gives

$$\partial_t f + \boldsymbol{v}\cdot\nabla|_{v_r,v_\theta,v_\varphi} f + \left(\frac{v_\theta^2 + v_\varphi^2}{r}\frac{\partial f}{\partial v_r} - \frac{v_r v_\theta}{r}\frac{\partial f}{\partial v_\theta} - \frac{v_r v_\varphi}{r}\frac{\partial f}{\partial v_\varphi}\right) = -\frac{1}{\tau}(f - f^{eq}). \tag{17}$$

It is clear that the term

$$\left(\frac{v_\theta^2 + v_\varphi^2}{r}\frac{\partial f}{\partial v_r} - \frac{v_r v_\theta}{r}\frac{\partial f}{\partial v_\theta} - \frac{v_r v_\varphi}{r}\frac{\partial f}{\partial v_\varphi}\right)$$

plays a role similar to that of the "force term" in the Boltzmann equation in Cartesian coordinates. It creates divergence or convergence effects in the flow system. As a first step, here we consider the simplest case where the thermodynamic nonequilibrium effects resulting from the pure geometric effects are much weaker than those resulting from other kinds of contributions. In such a case, we can use the approximation $f \approx f^{eq}$, when calculating the "force term". Such a treatment is reasonable when the flow behaviors under consideration are not close to the spherical center. If further we use the macroscopic condition $u_\theta = u_\varphi = 0$ for spherical symmetry, the final Boltzmann equation for the flow system with spherical symmetry becomes

$$\partial_t f + v_r\frac{\partial f}{\partial r} + \left[\frac{v_r v_\theta^2}{rT} + \frac{v_r v_\varphi^2}{rT} - \frac{\left(v_\theta^2 + v_\varphi^2\right)(v_r - u_r)}{rT}\right] f^{eq} = -\frac{1}{\tau}(f - f^{eq}). \tag{18}$$

2.2 Hydrodynamic model

The Navier–Stokes equations in Cartesian coordinates read

$$\frac{\partial\rho}{\partial t} + \frac{\partial(\rho u_\alpha)}{\partial x_\alpha} = 0, \tag{19a}$$

$$\frac{\partial(\rho u_\alpha)}{\partial t} + \frac{\partial(\rho u_\alpha u_\beta)}{\partial x_\beta} + \frac{\partial P\delta_{\alpha\beta}}{\partial x_\beta} = \frac{\partial\sigma_{\alpha\beta}}{\partial x_\beta}, \tag{19b}$$

$$\frac{\partial}{\partial t}\left(\rho E + \frac{1}{2}\rho u^2\right) + \frac{\partial}{\partial x_\alpha}\left[u_\alpha\left(\rho E + \frac{1}{2}\rho u^2 + P\right)\right] = \frac{\partial}{\partial x_\alpha}\left[Q_\alpha + u_\beta\sigma_{\alpha\beta}\right]. \tag{19c}$$

In the left-hand side of Eqs. (19a)–(19c), ρ, $\boldsymbol{u}$, $P = \rho RT$, $E{=}(D{+}n)RT/2$, T, and $\gamma{=}(D{+}n{+}2)/(D{+}n)$ are the hydrodynamic density, flow velocity, pressure, internal energy, temperature, and specific-heat ratio, respectively. R is the gas constant. $\alpha = x$, y, or z. $u^2 = \boldsymbol{u}\cdot\boldsymbol{u}$. D is the space dimension and n is the number of extra degrees of freedom. In the right-hand side of Eqs. (19b)–(19c),

$$\sigma_{\alpha\beta} = \mu\left[\frac{\partial u_\beta}{\partial r_\alpha} + \frac{\partial u_\alpha}{\partial r_\beta} - \left(\frac{2}{D} - \lambda\right)\frac{\partial u_\gamma}{\partial r_\gamma}\delta_{\alpha\beta}\right] \tag{20}$$

is the viscous stress and

$$Q_\alpha = \frac{2}{D}\kappa\frac{\partial e}{\partial r_\alpha} \tag{21}$$

is the heat flux. The two parameters μ and λ are the coefficients of viscosity and the parameter κ is the coefficient of heat conductivity. $e = DRT/2$ is the translational internal energy. It is clear that $P = 2\rho e/D$. When the viscosities and heat conductivity vanish, the hydrodynamic equations, Eqs. (19a)–(19c), become the Euler equations.

2.3 From the kinetic model to the hydrodynamic model

The Chapman–Enskog multiscale analysis shows that the Navier–Stokes equations, Eqs. (19a)–(19c), are the set of hydrodynamic equations from the Boltzmann BGK equation, (1), when only the first-order terms in the Knudsen number are taken into account. Among the infinite number of velocity kinetic moment relations of f^{eq}, only

$$\iint f^{eq}\mathrm{d}\boldsymbol{v}\mathrm{d}\boldsymbol{\eta} = \rho, \tag{22a}$$

$$\iint f^{eq}v_\alpha\mathrm{d}\boldsymbol{v}\mathrm{d}\boldsymbol{\eta} = \rho u_\alpha, \tag{22b}$$

$$\iint f^{eq}(v^2+\eta^2)\mathrm{d}\boldsymbol{v}\mathrm{d}\boldsymbol{\eta} = 2\rho\left(\frac{D+n}{D}e+\frac{u^2}{2}\right), \tag{22c}$$

$$\iint f^{eq}v_\alpha v_\beta\mathrm{d}\boldsymbol{v}\mathrm{d}\boldsymbol{\eta} = P\delta_{\alpha\beta}+\rho u_\alpha u_\beta, \tag{22d}$$

$$\iint f^{eq}(v^2+\eta^2)v_\alpha\mathrm{d}\boldsymbol{v}\mathrm{d}\boldsymbol{\eta} = 2\rho\left(\frac{D+n+2}{D}e+\frac{u^2}{2}\right)u_\alpha, \tag{22e}$$

$$\iint f^{eq}v_\alpha v_\beta v_\chi\mathrm{d}\boldsymbol{v}\mathrm{d}\boldsymbol{\eta} = \rho RT(u_\alpha\delta_{\beta\chi}+u_\beta\delta_{\alpha\chi}+u_\chi\delta_{\alpha\beta})+\rho u_\alpha u_\beta u_\chi, \tag{22f}$$

$$\iint f^{eq}(v^2+\eta^2)v_\alpha v_\beta\mathrm{d}\boldsymbol{v}\mathrm{d}\boldsymbol{\eta} = \frac{4}{D}\rho e\left(\frac{D+n+2}{D}e+\frac{u^2}{2}\right)\delta_{\alpha\beta}+2\rho u_\alpha u_\beta\left(\frac{D+n+4}{D}e+\frac{u^2}{2}\right), \tag{22g}$$

are needed in the Chapman–Enskog analysis, where $\boldsymbol{\eta}$ is a parameter describing the fluctuating velocity in the n extra degrees of freedom, $\eta^2 = \boldsymbol{\eta}\cdot\boldsymbol{\eta}$, and

$$f^{eq}(\boldsymbol{v},\boldsymbol{\eta}) = \rho\left(\frac{1}{2\pi RT}\right)^{(D+n)/2}\exp\left[-\frac{(v-u)^2+\eta^2}{2RT}\right]. \tag{23}$$

The Chapman–Enskog analysis gives the following constitutive relations for the Navier–Stokes model, (19a)–(19c):

$$\mu = \frac{2}{D}\rho e\tau, \quad \lambda = \frac{2n}{D(D+n)}, \quad k = \frac{D+n+2}{D}\rho e\tau.$$

Under spherical symmetry, the Navier–Stokes equations read

$$\begin{aligned}
&\partial_t\rho+\left(\partial_t+\frac{2}{r}\right)(\rho u_r) = 0,\\
&\partial_t(\rho u_r)+\left(\partial_r+\frac{2}{r}\right)(\rho u_r u_r)+\partial_r p = \partial_r\left\{\mu\left[\left(2-\frac{2}{D}\right)\partial_r u_r+\lambda\partial_r u_r\right]\right\},\\
&\partial_t\left[\rho\left(E+\frac{u_r^2}{2}\right)\right]+\left(\partial_r+\frac{2}{r}\right)\left[\rho u_r\left(E+\frac{u_r^2}{2}\right)\right]+\left(\partial_r+\frac{2}{r}\right)(pu_r) = \partial_r\left\{\frac{2}{D}\kappa\partial_r e+u_r\mu\left[\left(2-\frac{2}{D}\right)\partial_r u_r+\lambda\partial_r u_r\right]\right\},
\end{aligned} \tag{24}$$

which can be recovered from the kinetic model (18).

2.4 Measurements of nonequilibrium effects

The Chapman–Enskog multiscale analysis tells us that, as the simplest hydrodynamic model of a fluid system, the Euler equations completely ignore the TNE behavior. The Navier–Stokes equations describe the TNE behavior via the viscosity and heat conductivity terms. The Euler model works successfully when we consider the fluid system in a time scale t_0 that is large enough compared with the thermodynamic relaxation time τ. Besides being applicable to normal high-speed compressible flows, the Euler model works also for solid materials under a

strong shock. From the mechanical side, compared with the shocking strength, the material strength and viscous stress are negligible. Consequently, the Euler model works better with increasing shock strength. From the aspect of time scales, when we study the shock process, the time scale t_0 used is generally small enough compared with the time scale t_h for heat conduction and large enough compared with the thermodynamic relaxation time τ. In other words, during the time interval under investigation, heat conduction does not have time to occur significantly and consequently its effects are negligible. For the objective system where the thermodynamic relaxation time τ is fixed, if we decrease the observing time scale t_0, we find more TNE effects. The Boltzmann kinetic model can be used to investigate both the hydrodynamic and thermodynamic behaviors.

Following the seven moment relations (22a)–(22g) used in recovering the Navier–Stokes equations, we define the following moments:

$$\boldsymbol{M}^*_m(f,\boldsymbol{v}) = \iint f\boldsymbol{v}^m \mathrm{d}\boldsymbol{v}\mathrm{d}\boldsymbol{\eta}, \tag{25a}$$

$$\boldsymbol{M}^*_{m,n}(f,\boldsymbol{v}) = \iint f(\boldsymbol{v}\cdot\boldsymbol{v}+\eta^2)^{(m-n)/2}\boldsymbol{v}^n \mathrm{d}\boldsymbol{v}\mathrm{d}\boldsymbol{\eta}, \tag{25b}$$

where $\boldsymbol{M}^*_n$ means an nth-order tensor and $\boldsymbol{M}^*_{m,n}$ means an nth-order tensor contracted from an mth-order tensor. For the case of central moments, the variable $\boldsymbol{v}$ is replaced with $\boldsymbol{v}^* = \boldsymbol{v} - \boldsymbol{u}$. It is clear that $\boldsymbol{M}^*_0$ and $\boldsymbol{M}^*_{2,0}$ are scalars. Each of them has only one component. $\boldsymbol{M}^*_1$ and $\boldsymbol{M}^*_{3,1}$ are vectors. Each of them has two independent components in the two-dimensional case or three independent components in the three-dimensional case. $\boldsymbol{M}^*_2$ and $\boldsymbol{M}^*_{4,2}$ are second-order tensors. Each of them has three independent components in the two-dimensional case or six independent components in the three-dimensional case. $\boldsymbol{M}^*_3$ is a third-order tensor and has 4 independent components in the two-dimensional case or 10 independent components in the three-dimensional case. Therefore, constraints (22a)–(22g) are in fact 16 linear equations in f^{eq} in the two-dimensional case and 30 linear equations in f^{eq} in three-dimensional case. We further define

$$\boldsymbol{\Delta}^*_{m,n}(\boldsymbol{v}) = \boldsymbol{M}^*_{m,n}(f,\boldsymbol{v}) - \boldsymbol{M}^*_{m,n}(f^{eq},\boldsymbol{v}). \tag{26}$$

It is clear that $\boldsymbol{\Delta}^*_0(\boldsymbol{v}) = \boldsymbol{0}$, $\boldsymbol{\Delta}^*_1(\boldsymbol{v}) = \boldsymbol{0}$, and $\boldsymbol{\Delta}^*_{2,0}(\boldsymbol{v}) = \boldsymbol{0}$ as a result of mass, momentum, and energy conservation. Except for these three components, the quantity $\boldsymbol{\Delta}^*_{m,n}(\boldsymbol{v})$ works as a measure for the deviation of the system from its thermodynamic equilibrium. The information of flow velocity $\boldsymbol{u}$ is taken into account in the definition (26). Similarly,

$$\boldsymbol{\Delta}^*_{m,n}(\boldsymbol{v}^*) = \boldsymbol{M}^*_{m,n}(f,\boldsymbol{v}^*) - \boldsymbol{M}^*_{m,n}(f^{eq},\boldsymbol{v}^*). \tag{27}$$

Except for $\boldsymbol{\Delta}^*_0(\boldsymbol{v}^*)$, $\boldsymbol{\Delta}^*_1(\boldsymbol{v}^*)$, and $\boldsymbol{\Delta}^*_{2,0}(\boldsymbol{v}^*)$, the quantity $\boldsymbol{\Delta}^*_{m,n}(\boldsymbol{v}^*)$ works as a measure for the deviation of the system from its thermodynamic equilibrium, where only the thermal fluctuations of the molecules are considered.

3 Discrete Boltzmann models for systems with spherical symmetry

There are two key techniques used in constructing the DBM with force terms. The first is to calculate the velocity derivative of f, $\partial f/\partial \boldsymbol{v}$, before discretizing the particle velocity space. As a first step, one can consider the case where f can be approximated by f^{eq} in the force term. The second technique is to write the discrete equilibrium distribution function f^{eq}_i as a function of the discrete velocities, where i is the index of the discrete velocity.

For constructing the DBM for systems with spherical symmetry, we use Eq. (18). We have

$$\partial_t f_i + v_{ir}\frac{\partial f_i}{\partial r} + \left[\frac{v_{ir}v^2_{i\theta}}{rT} + \frac{v_{ir}v^2_{i\varphi}}{rT} - \frac{(v^2_{i\theta}+v^2_{i\varphi})(v_{ir}-u)}{rT}\right] f^{eq}_i = -\frac{1}{\tau}(f_i - f^{eq}_i), \tag{28}$$

where f_i (f^{eq}_i) is the discrete (equilibrium) distribution function and v_i is the ith discrete velocity, with $i = 1,\ldots,N$, where N is the total number of the discrete velocity points.

The fundamental requirement for a DBM is that it should recover the same set of hydrodynamic equations as those given by the original continuous Boltzmann equation. The Chapman–Enskog multiscale analysis shows that, only if the seven moment relations (22a)–(22g) can be calculated equally in the summation form as follows:

$$\rho = \sum_{i=1}^{N} f^{eq}_i = \sum_{i=1}^{N} f_i, \tag{29a}$$

$$\rho u_\alpha = \sum_{i=1}^{N} f^{eq}_i v_{i\alpha} = \sum_{i=1}^{N} f_i v_{i\alpha}, \tag{29b}$$

$$2\rho\left(\frac{D+n}{D}e + \frac{u^2}{2}\right) = \sum_{i=1}^{N} f^{eq}_i(v^2_i+\eta^2_i) = \sum_{i=1}^{N} f_i(v^2_i+\eta^2_i), \tag{29c}$$

$$P\delta_{\alpha\beta}+\rho u_\alpha u_\beta=\sum_{i=1}^{N} f_i^{eq} v_{i\alpha}v_{i\beta}, \tag{29d}$$

$$2\rho\left(\frac{D+n+2}{D}e+\frac{u^2}{2}\right)u_\alpha=\sum_{i=1}^{N} f_i^{eq}(v_i^2+\eta_i^2)v_{i\alpha}, \tag{29e}$$

$$\rho RT(u_\alpha\delta_{\beta\chi}+u_\beta\delta_{\alpha\chi}+u_\chi\delta_{\alpha\beta})+\rho u_\alpha u_\beta u_\chi=\sum f_i^{eq} v_{i\alpha}v_{i\beta}v_{i\chi}, \tag{29f}$$

$$\frac{4}{D}\rho e\left(\frac{D+n+2}{D}e+\frac{u^2}{2}\right)\delta_{\alpha\beta}+2\rho u_\alpha u_\beta\left(\frac{D+n+4}{D}e+\frac{u^2}{2}\right)=\sum f_i^{eq}(v_i^2+\eta_i^2)v_{i\alpha}v_{i\beta}, \tag{29g}$$

can the Navier–Stokes model, (19a)–(19c), be recovered from the DBM, (28). Following the same idea as in definitions (25a)–(25b), we define the following moments of the discrete distribution function f_i:

$$\boldsymbol{M}_m^*(f_i,\boldsymbol{v}_i)=\sum_{i=1}^{N}\boldsymbol{v}_i^m f_i, \tag{30a}$$

$$\boldsymbol{M}_{m,n}^*(f_i,\boldsymbol{v}_i)=\sum_{i=1}^{N} f_i(\boldsymbol{v}_i\cdot\boldsymbol{v}_i+\eta_i^2)^{(m-n)/2}\boldsymbol{v}_i^n, \tag{30b}$$

where $\boldsymbol{M}_n$ means an nth-order tensor and $\boldsymbol{M}_{m,n}$ means an nth-order tensor contracted from an mth-order tensor. For the case of central moments, the variable $\boldsymbol{v}$ is replaced with $\boldsymbol{v}^*=\boldsymbol{v}-\boldsymbol{u}$. Constraints (29a)–(29g) are in fact 16 linear equations in f_i^{eq} in the two-dimensional case and 30 linear equations in f_i^{eq} in the three-dimensional case. Following the same idea as in definitions (26) and (27), we further define

$$\boldsymbol{\Delta}_{m,n}(\boldsymbol{v}_i)=\boldsymbol{M}_{m,n}(f_i,\boldsymbol{v}_i)-\boldsymbol{M}_{m,n}(f_i^{eq},\boldsymbol{v}_i), \tag{31}$$

$$\boldsymbol{\Delta}_{m,n}(\boldsymbol{v}_i^*)=\boldsymbol{M}_{m,n}(f_i,\boldsymbol{v}_i^*)-\boldsymbol{M}_{m,n}(f_i^{eq},\boldsymbol{v}_i^*). \tag{32}$$

Except for $\boldsymbol{\Delta}_0$, $\boldsymbol{\Delta}_1$, and $\boldsymbol{\Delta}_{2,0}$, the quantity $\boldsymbol{\Delta}_{m,n}$ works as a measure for the deviation of the system from its thermodynamic equilibrium.

Constraints (29a)–(29g) can also be rewritten as

$$\hat{\boldsymbol{f}}^{eq}=\boldsymbol{C}\cdot\boldsymbol{f}^{eq}, \tag{33}$$

where $\hat{\boldsymbol{f}}^{eq}=[\hat{f}_k^{eq}]^T$ and $\boldsymbol{f}^{eq}=[f_k^{eq}]^T$ are column vectors with $k=1,2,\ldots,N$, and $\boldsymbol{C}$ is an $N\times N$ matrix whose components are determined by $\boldsymbol{v}_i$ if the parameter η_i is fixed. It is clear that

$$\boldsymbol{f}^{eq}=\boldsymbol{C}^{-1}\cdot\hat{\boldsymbol{f}}^{eq}. \tag{34}$$

Obviously, in choosing the DVM, one must ensure the existence of $\boldsymbol{C}^{-1}$. The specific choice of the DVM depends on the compromise among the following points: (i) numerical efficiency, (ii) numerical stability, and (iii) local symmetry of relevant kinetic moments. We work in the frame in which the particle mass $m=1$ and the gas constant $R=1$.

If we require the DBM to recover the Navier–Stokes equations in the continuum limit, the DBM needs a DVM with three dimensions.

3.1 Case with $\gamma=5/3$

We first consider the simple case where the specific-heat ratio is fixed at $\gamma=5/3$. We set $\eta_i=0$ and $n=0$ in constraint (29g). Among the seven moment constraints, (29a)–(29g), only five are independent. We do not use constraints (29c) and (29e). The five independent constraints can be rewritten as 26 independent linear equations in f_i^{eq}. Now, we fix the components $\hat{f}_k^{eq}$ of $\hat{\boldsymbol{f}}^{eq}$. Here $N=26$.

From constraint (29a), we have $\hat{f}_1^{eq}=\rho$. From constraint (29b), we have $\hat{f}_2^{eq}=\rho u_r$, $\hat{f}_3^{eq}=\rho u_\theta$, and $\hat{f}_4^{eq}=\rho u_\varphi$. From constraint (29d), we have $\hat{f}_5^{eq}=P+\rho u_r^2$, $\hat{f}_6^{eq}=\rho u_r u_\theta$, $\hat{f}_7^{eq}=\rho u_r u_\varphi$, $\hat{f}_8^{eq}=P+\rho u_\theta^2$, $\hat{f}_9^{eq}=\rho u_\theta u_\varphi$, and $\hat{f}_{10}^{eq}=P+\rho u_\varphi^2$. From constraint (29f), we have $\hat{f}_{11}^{eq}=\rho[T(3u_r)+u_r^3]$, $\hat{f}_{12}^{eq}=\rho(Tu_\theta+u_r^2u_\theta)$, $\hat{f}_{13}^{eq}=\rho(Tu_\varphi+u_r^2u_\varphi)$, $\hat{f}_{14}^{eq}=\rho(Tu_r+u_ru_\theta^2)$, $\hat{f}_{15}^{eq}=\rho(u_ru_\theta u_\varphi)$, $\hat{f}_{16}^{eq}=\rho(Tu_r+u_ru_\varphi^2)$, $\hat{f}_{17}^{eq}=\rho[T(3u_\theta)+u_\theta^3]$, $\hat{f}_{18}^{eq}=\rho[Tu_\varphi+u_\theta^2u_\varphi]$, $\hat{f}_{19}^{eq}=\rho[Tu_\theta+u_\varphi^2u_\theta]$, and $\hat{f}_{20}^{eq}=\rho[T(3u_\varphi)+u_\varphi^3]$. From constraint (29g), we have $\hat{f}_{21}^{eq}=\rho T(5T+u^2)+\rho u_r^2(7T+u^2)$, $\hat{f}_{22}^{eq}=\rho u_ru_\theta(7T+u^2)$, $\hat{f}_{23}^{eq}=\rho u_ru_\varphi(7T+u^2)$, $\hat{f}_{24}^{eq}=\rho T(5T+u^2)+\rho u_\theta^2(7T+u^2)$, $\hat{f}_{25}^{eq}=\rho u_\theta u_\varphi(7T+u^2)$, and $\hat{f}_{26}^{eq}=\rho T(5T+u^2)+2\rho u_\varphi^2(7T+u^2)$.

Because the system is spherically symmetric on the macroscopic scale, $u_\theta=u_\varphi=0$ and $u^2=u_r^2$ in the above expressions for $\hat{\boldsymbol{f}}^{eq}=[\hat{f}_1^{eq},\hat{f}_2^{eq},\cdots,\hat{f}_N^{eq}]^T$.

The components of the matrix $\boldsymbol{C}=[\boldsymbol{C}_k]=[C_{ki}]$ should be fixed in the same sequence, where $k=1,2,\ldots,26$ and $i=1,2,\ldots,26$. From constraint (29a), we have $C_{1i}=1$. From constraint (29b), we have $C_{2i}=v_{ir}$, $C_{3i}=v_{i\theta}$, and $C_{4i}=v_{i\varphi}$. From constraint (29d), we have $C_{5i}=v_{ir}^2$, $C_{6i}=v_{ir}v_{i\theta}$, $C_{7i}=v_{ir}v_{i\varphi}$, $C_{8i}=v_{i\theta}^2$, $C_{9i}=v_{i\theta}v_{i\varphi}$, and $C_{10i}=v_{i\varphi}^2$. From constraint (29f), we have $C_{11i}=v_{ir}^3$, $C_{12i}=v_{ir}^2v_{i\theta}$, $C_{13i}=v_{ir}^2v_{i\varphi}$, $C_{14i}=v_{ir}v_{i\theta}^2$, $C_{15i}=v_{ir}v_{i\theta}v_{i\varphi}$, $C_{16i}=v_{ir}v_{i\varphi}^2$, $C_{17i}=v_{i\theta}^3$, $C_{18i}=v_{i\theta}^2v_{i\varphi}$, $C_{19i}=v_{i\theta}v_{i\varphi}^2$, and $C_{20i}=v_{i\varphi}^3$.

From constraint (29g), we have $C_{21i} = (v_{ir}^2+v_{i\theta}^2+v_{i\varphi}^2)v_{ir}^2$, $C_{22i} = (v_{ir}^2+v_{i\theta}^2+v_{i\varphi}^2)v_{ir}v_{i\theta}$, $C_{23i} = (v_{ir}^2+v_{i\theta}^2+v_{i\varphi}^2)v_{ir}v_{i\varphi}$, $C_{24i} = (v_{ir}^2+v_{i\theta}^2+v_{i\varphi}^2)v_{i\theta}^2$, $C_{25i} = (v_{ir}^2+v_{i\theta}^2+v_{i\varphi}^2)v_{i\theta}v_{i\varphi}$, and $C_{26i} = (v_{ir}^2+v_{i\theta}^2+v_{i\varphi}^2)v_{i\varphi}^2$.

An example of the three-dimensional 26-velocity (D3V26) DVM is as follows:

$$\boldsymbol{v}_i = \begin{cases} (0,\pm1,\pm1)c_1, & i = 1,\ldots,4, \\ (\pm1,0,\pm1)c_1, & i = 5,\ldots,8, \\ (\pm1,\pm1,0)c_1, & i = 9,\ldots,12, \end{cases} \tag{35a}$$

$$\boldsymbol{v}_i = \{ (\pm1,\pm1,\pm1)c_2, \quad i = 13,\ldots,20, \tag{35b}$$

$$\boldsymbol{v}_i = \begin{cases} (\pm1,0,0)c_3, & i = 21,22, \\ (0,\pm1,0)c_3, & i = 23,24, \\ (0,0,\pm1)c_3, & i = 25,26. \end{cases} \tag{35c}$$

The schematic of the discrete velocity model is shown in Fig. 2. The expressions for the inverse of the matrix $\boldsymbol{C}$, $\boldsymbol{C}^{-1} = [\boldsymbol{C}_k^{-1}]$, can be easily obtained by using MATLAB software, then a specific example of the DVM is formulated.

Up to this step, a specific discretization of the velocity space has been performed. Consequently, the DBM for a system with spherical symmetry and $\gamma = 5/3$ has been constructed. The spatial and temporal derivatives of the distribution function in the kinetic model can be calculated in the normal way. If we are not interested in the extra degrees of freedom other than the translational ones, the formulated DBM can be used to study the hydrodynamic and thermodynamic behaviors of the compressible flow system. The computational domain in this work can be found in Fig. 3, where the projection of the computational domain in two-dimensional space is shown. In the rest of this paper, $r - r_0$ is used as the label of the spatial axis, where r_0 is the distance between the computational domain and the center of the sphere.

First, we simulate a Sod shock tube problem using the DBM where the "force term" in Eq. (28) does not exist. Such a test can be used to check the validity of the DVM. In addition, the case with no "force term" corresponds to the case in which the value of r_0 is so large that geometric effects are negligible. The results are shown in Fig. 4. The Riemann solutions are also plotted for comparison. The calculated results show that the new DVM (D3V26) is applicable and that the new DBM model can capture the discontinuous interface.

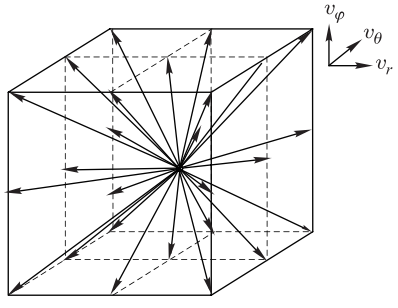

Fig. 2 Schematic of the discrete velocity model (D3V26).

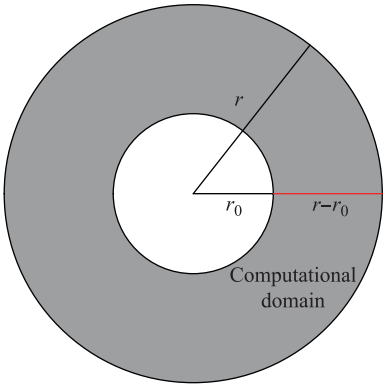

Fig. 3 Schematic of the computational domain (gray area).

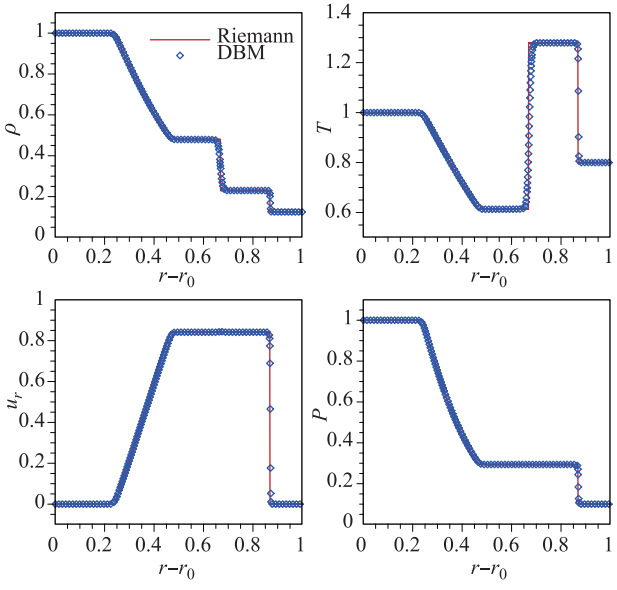

Fig. 4 Profile of macroquantities for Sod shock tube with $\gamma = 5/3$.

Then, to check the geometric effects, two cases of propagating shock waves with Mach number $Ma = 1.5$ along the radial direction are simulated. In the first case, the shock wave propagates outward so that divergence occurs. Several cases with different values of r_0 are simulated. The results are shown in Fig. 5(a). For easy understanding, three-dimensional contour maps of hydrodynamic quantities at a certain time for the case with $r_0 = 0.5$ are given in Fig. 6. Figure 5(a) shows the variation of wavefront position with time. From the figure, we can find that the propagation speed of the shock wave de-

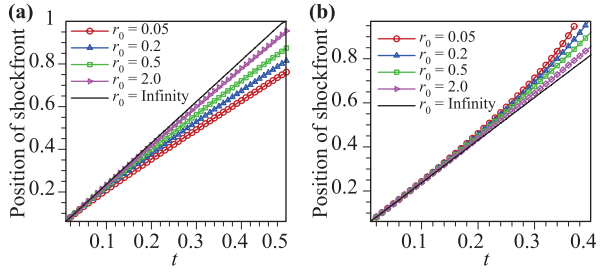

Fig. 5 The position of shock wavefront versus time for the case with $\gamma = 5/3$. **(a)** Shock wave propagates outward (explosion). **(b)** Shock wave propagates inward (implosion).

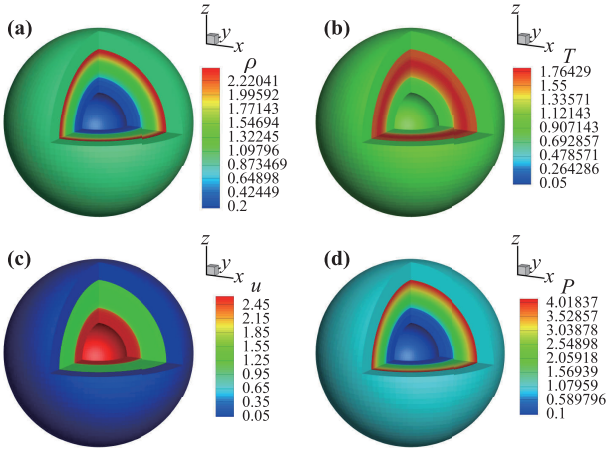

Fig. 6 The contour maps of macroquantities for shock wave propagating outward for $r_0 = 0.5$ at $t = 0.9$. **(a)** Contour map of density, ρ. **(b)** Contour map of temperature, T. **(c)** Contour map of velocity, u. **(d)** Contour map of pressure, P.

creases with time as a result of the divergence. Besides, the smaller r_0 value gives a faster decrease of propagation speed. The second case is that in which the shock wave propagates inward so that convergence plays a role. Figure 5(b) shows the variation of wavefront position with time. The propagation speed of the shock wave increases with time as a result of the convergence, and the smaller r_0 value gives a faster increase of propagation speed.

The above simulation results and analysis show that the new model can well describe the geometric effects of flows with spherical symmetry.

3.2 Case with flexible γ

For the case with flexible specific-heat ratio γ, if we are interested only in the hydrodynamic behavior, we can use the simulation results of the DBM formulated in the last subsection. We just get the number n of the extra degree of freedom using its relation to γ, then obtain the total internal energy E using its definition. If we are interested also in the thermodynamic nonequilibrium behavior, we need to continue the formulation of the DBM.

To model the case with flexible γ, we resort to the parameter $\boldsymbol{\eta}$ to describe the contribution of extra degrees of freedom. The distribution function f with n extra degrees of freedom can be replaced by g and h, and the equilibrium distribution function f^{eq} in Eq. (23) is replaced by g^{eq} and h^{eq}, where

$$g = \int f \mathrm{d}\boldsymbol{\eta}, \tag{36a}$$

$$h = \int f \eta^2 \mathrm{d}\boldsymbol{\eta}, \tag{36b}$$

$$g^{eq} = \int f^{eq} \mathrm{d}\boldsymbol{\eta}, \tag{36c}$$

$$h^{eq} = \int f^{eq} \eta^2 \mathrm{d}\boldsymbol{\eta}. \tag{36d}$$

The functions g and g^{eq} recover to f and f^{eq} when there are no extra degrees of freedom (i.e., $\gamma = 5/3$). The evolution equation of f in Eq. (18) becomes two evolution equations of g and h. They read

$$\partial_t g + v_r \frac{\partial g}{\partial r} + \left[\frac{v_r v_\theta^2}{rT} + \frac{v_r v_\varphi^2}{rT} - \frac{(v_\theta^2 + v_\varphi^2)(v_r - u_r)}{rT}\right] g^{eq} = -\frac{1}{\tau}(g - g^{eq}), \tag{37a}$$

$$\partial_t h + v_r \frac{\partial h}{\partial r} + \left[\frac{v_r v_\theta^2}{rT} + \frac{v_r v_\varphi^2}{rT} - \frac{(v_\theta^2 + v_\varphi^2)(v_r - u_r)}{rT}\right] h^{eq} = -\frac{1}{\tau}(h - h^{eq}), \tag{37b}$$

where

$$g^{eq}(\boldsymbol{v}) = \rho \left(\frac{1}{2\pi RT}\right)^{D/2} \exp\left[-\frac{(v-u)^2}{2RT}\right], \tag{38a}$$

$$h^{eq} = nTg^{eq}. \tag{38b}$$

As a result, the value of f_i^{eq} solved before for the case with $\gamma = 5/3$ can be used as g_i^{eq} here. Then h_i^{eq} can be solved by

$$h_i^{eq} = nTg_i^{eq}. \tag{39}$$

In this modeling approach, $\boldsymbol{\eta}$ does not need to be discretized at all, and the moments in Eqs. (30a)–(30b) are

calculated by

$$\boldsymbol{M}_m(f_i,\boldsymbol{v}_i)=\sum_{i=1}^{N} g_i\boldsymbol{v}_i^m, \tag{40a}$$

$$\boldsymbol{M}_{m,n}(f_i,\boldsymbol{v}_i)=\sum_{i=1}^{N}(g_i\boldsymbol{v}_i\cdot\boldsymbol{v}_i+h_i)^{(m-n)/2}\boldsymbol{v}_i^n. \tag{40b}$$

The definitions of $\boldsymbol{\Delta}_{m,n}(\boldsymbol{v}_i)$ and $\boldsymbol{\Delta}_{m,n}(\boldsymbol{v}_i^*)$ in Eqs. (31) and (32) will stay the same and work as a measure for the deviation of the system from its thermodynamic equilibrium. Up to this step, a DBM with D3V26 for a system with flexible specific-heat ratio γ has been formulated.

To test the flexibility of γ, Sod shock tube problems with two different values of γ were simulated. The specific-heat ratio for one case was $\gamma=1.4$, which means there are two extra degrees of freedom ($n=2$), and for the other case it is $\gamma=1.5$, which means there is only one extra degree of freedom ($n=1$). First, we ignore geometric effects. The results for the two cases are shown in Figs. 7 and 8, respectively. The results are in good agreement with the Riemann solutions, which verifies the validity of the new model.

Then, a shock wave with $Ma=3$ propagating along the radial direction was simulated for the case with $\gamma=1.4$ (i.e., $n=2$). First, we assumed that the shock wave starts at infinity from the center of the sphere, so that the "force term" in Eqs. (37a) and (37b) are negligible. Profiles of the macroquantities, including ρ, u, and P around the wavefront, at a certain time are shown in Fig. 9(a). The macroquantities on the two sides of the wavefront satisfy the Hugoniot relations of the shock wave. The corresponding nonequilibrium quantities, including $\Delta_{2,rr}(v_i)$, $\Delta_{3,rrr}(v_i)$, $\Delta_{3,1,r}(v_i)$, and $\Delta_{4,2,rr}(v_i)$,

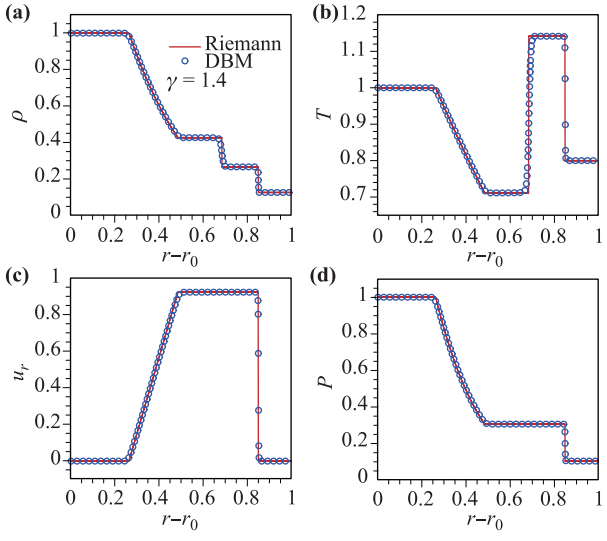

Fig. 7 Profiles of macroquantities for Sod shock tube with $\gamma=1.4$ ($n=2$).

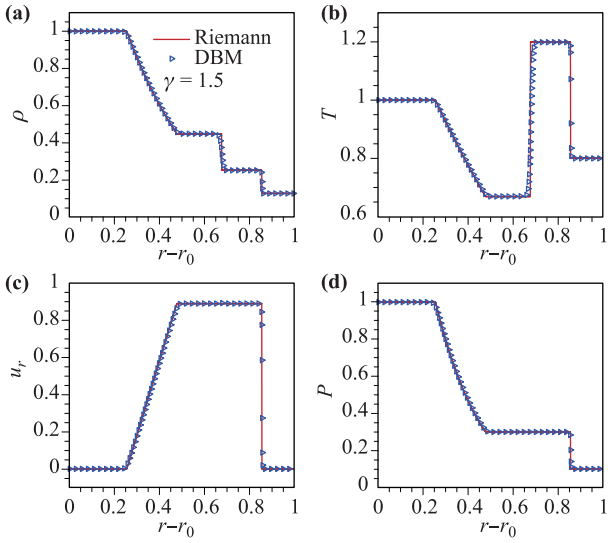

Fig. 8 Profiles of macroquantities for Sod shock tube with $\gamma=1.5$ ($n=1$).

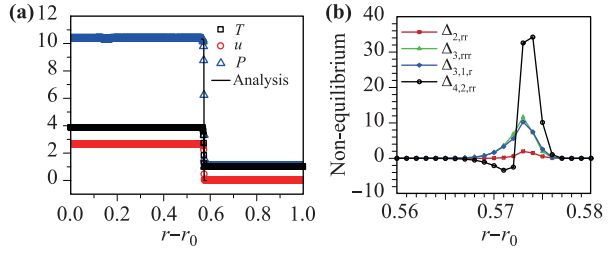

Fig. 9 Profiles of macroquantities and nonequilibrium effects around shock wavefront for the case with $Ma=3.0$ and $\gamma=1.4$. **(a)** Profiles of ρ, u, and P. The symbols indicate the results of DBM and solid lines are solutions based on Hugoniot relations of shock wave. **(b)** Profiles of nonequilibrium effects around shock wavefront.

around the wavefront are plotted in Fig. 9(b). Because the shock propagates in the radial direction, only one component in the r direction is considered for each of the four kinds of nonequilibrium quantities. From Fig. 9(b), we can get nonequilibrium characteristics from a different point of view (other than from the viscous stress and heat flux), which cannot be provided by the traditional Navier–Stokes equations.

Then, geometric effects were taken into account. Shock waves propagating outward and inward were both simulated. The evolutions of wavefront positions are shown in Figs. 10(a) and (b), respectively.

From Fig. 10(a), it can be seen the shock wave has a constant propagation speed for $r_0=\infty$, which corresponds to the case in Fig. 9. For the shock wave propagating outward, the propagation speed decreases with time, and the smaller r_0 value gives a faster decrease, which indicates a stronger "force" caused by geometric

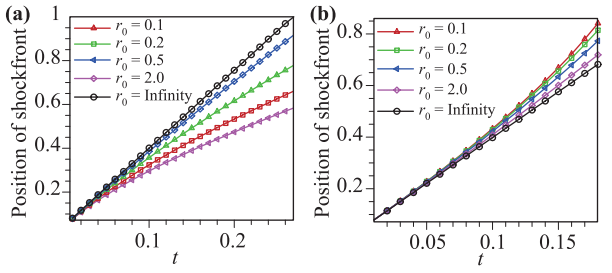

Fig. 10 The position of shock wavefront versus time for the case with $\gamma = 1.4$. **(a)** Shock wave propagates outward. **(b)** Shock wave propagates inward.

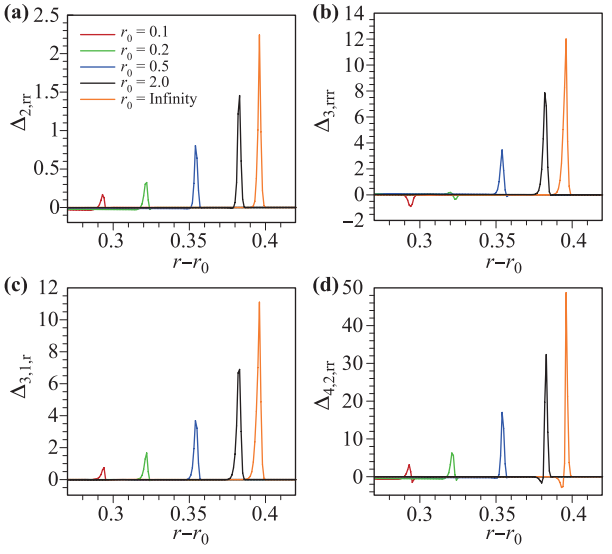

Fig. 11 The nonequilibrium quantities around wavefront for explosion.

effects. The shock wave propagating inward has similar characteristics, except that the propagation speed increases with time as a result of convergence.

3.3 Thermodynamic nonequilibrium characteristics in explosion and implosion

The nonequilibrium quantities around the wavefront for a shock propagating outward (i.e., an explosion) at a certain time are plotted in Fig. 11. In this case, the divergence effect plays the role of a resistance force. It decreases the propagation speed and reduces the nonequilibrium strength. It can be found in Fig. 11(b) that a smaller r_0 value, which means a stronger divergence effect, may even change the direction of the deviation from the equilibrium state for $\Delta_{3,rrr}$.

More discussion on the reasonability of the approximation $f \approx f^{eq}$ in treating the term for pure geometric effects in Eq. (17) is warranted. When the flow under consideration is not close to the spherical center, the error induced by the approximation when calculating the "force term" is relatively very small compared with the "convective term". The comparison can be made in moment space.

First, the "force term" in moment space is defined as

$$\boldsymbol{M}_n^{Geo}(f)=\int\left(\frac{v_\theta^2+v_\varphi^2}{r}\frac{\partial f}{\partial v_r}-\frac{v_r v_\theta}{r}\frac{\partial f}{\partial v_\theta}-\frac{v_r v_\varphi}{r}\frac{\partial f}{\partial v_\varphi}\right)\boldsymbol{v}^n \mathrm{d}\boldsymbol{v}, \tag{41}$$

where the subscript n in $\boldsymbol{M}_n^{Geo}(f)$ indicates the nth-order moment. Then the error induced by the approximation $f \approx f^{eq}$ in moment space is

$$\boldsymbol{\Delta}_n^{Geo} = \boldsymbol{M}_n^{Geo}(f) - \boldsymbol{M}_n^{Geo}(f^{eq}). \tag{42}$$

Similarly, the convective term in moment space is defined as

$$\boldsymbol{M}_n^{Con}(f) = \int(\boldsymbol{v}\cdot\nabla f)\boldsymbol{v}^n \mathrm{d}\boldsymbol{v}. \tag{43}$$

The ratio $\Delta_n^{Geo}/M_n^{Con}(f)$ measures the relative error induced by $f \approx f^{eq}$ when calculating the "force term" with respect to the convective term. Because the density, momentum, and energy are the zeroth-order, first-order, and second-order moments, respectively, only Δ_0^{Geo}/M_0^{Con}, $\Delta_{1,r}^{Geo}/M_{1,r}^{Con}$, and $\Delta_{2,0}^{Geo}/M_{2,0}^{Con}$ are investigated here. The subscript "2, 0" indicates that $\Delta_{2,0}^{Geo}$ (or $M_{2,0}^{Con}$) is a zeroth-order tensor (i.e., scalar) contracted from the second-order tensor. According to the definition of $\boldsymbol{\Delta}_n^{Geo}$ and $\boldsymbol{M}_n^{Con}(f)$, we can get that

$$\frac{\Delta_0^{Geo}}{M_0^{Con}} = \frac{\int 2\frac{v_r}{r}(f-f^{eq})\mathrm{d}\boldsymbol{v}}{\int(\boldsymbol{v}\cdot\nabla f)\mathrm{d}\boldsymbol{v}}, \tag{44}$$

$$\frac{\Delta_{1,r}^{Geo}}{M_{1,r}^{Con}} = \frac{\int\left(-\frac{v_\theta^2+v_\varphi^2}{r}+2\frac{v_r v_\theta}{r}+2\frac{v_r v_\varphi}{r}\right)(f-f^{eq})\mathrm{d}\boldsymbol{v}}{\frac{\partial M_{2,rr}}{\partial r}+\frac{\partial M_{2,r\theta}}{\partial\theta}+\frac{\partial M_{2,r\varphi}}{\partial\varphi}}, \tag{45}$$

$$\frac{\Delta_{2,0}^{Geo}}{M_{2,0}^{Con}} = \frac{\int\left[\left(-2v_r\frac{v_\theta^2+v_\varphi^2}{r}\right)+\frac{v_r^3+3v_r v_\theta^2+v_r v_\varphi^2}{r}+\frac{v_r^3+v_r v_\theta^2+3v_r v_\varphi^2}{r}\right](f-f^{eq})\mathrm{d}\boldsymbol{v}}{\frac{\partial M_{3.1,r}}{\partial r}+\frac{\partial M_{3.1,\theta}}{\partial\theta}+\frac{\partial M_{3.1,\varphi}}{\partial\varphi}}. \tag{46}$$

It is obvious that Δ_0^{Geo}/M_0^{Con} is always equal to zero. Therefore, only $\Delta_{1,r}^{Geo}/M_{1,r}^{Con}$ and $\Delta_{2,0}^{Geo}/M_{2,0}^{Con}$ are used to measure the relative error of the "force term." The profiles of $\Delta_{1,r}^{Geo}/M_{1,r}^{Con}$, $\Delta_{1,r}^{Geo}$, and $M_{1,r}^{Con}$ for the case with $r_0 = 0.1$ are shown in Fig. 12(a). It can be seen that $\Delta_{1,r}^{Geo}$ is so small compared with $M_{1,r}^{Con}$ that it nearly can be ignored even for such a small r_0. From Fig. 12(b) we can see the $\Delta_{2,0}^{Geo}$ is also nearly negligible compared with $M_{2,0}^{Con}$. Besides, with the increase of r_0, the effects become weaker, with Δ_n^{Geo} becoming more negligible compared with M_n^{Con}, which is verified in Fig. 13. From Fig. 13 we can conclude that the error Δ_n^{Geo} is negligible compared with M_n^{Con} when $r_0 \geq 0.1$.

For a shock propagating inward (i.e., an implosion), the nonequilibrium quantities at a certain time are shown in Fig. 14. In this case, the convergence effect accelerates the propagation speed of the shock wave, thereby also strengthen the nonequilibrium effects around the wavefront. A smaller r_0 corresponds to a stronger nonequilibrium. Unlike the shock propagating outward, no change of the direction for the deviation from the thermodynamic equilibrium state is found.

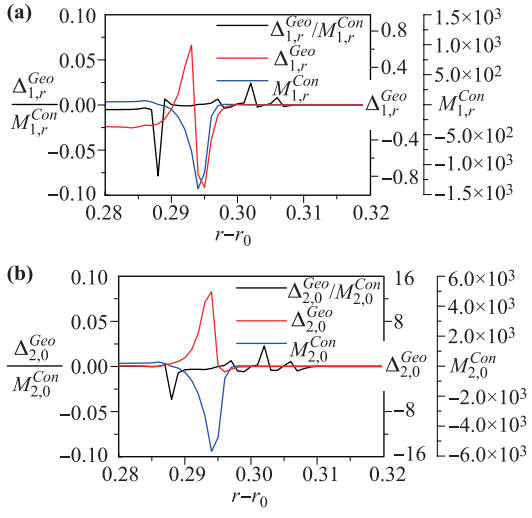

Fig. 12 The profiles of **(a)** $\Delta_{1,r}^{Geo}/M_{1,r}^{Con}$, $\Delta_{1,r}^{Geo}$, and $M_{1,r}^{Con}$ and **(b)** $\Delta_{2,0}^{Geo}/M_{2,0}^{Con}$, $\Delta_{2,0}^{Geo}$, and $M_{2,0}^{Con}$ around the shock wave front for the case with $r_0 = 0.1$ (explosion).

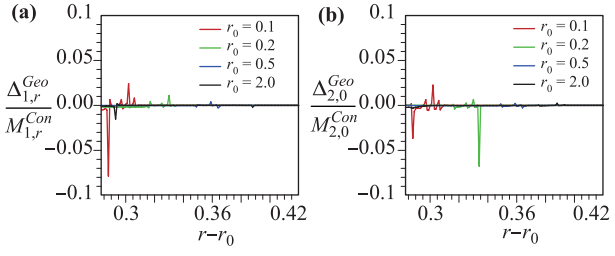

Fig. 13 The profiles of **(a)** $\Delta_{1,r}^{Geo}/M_{1,r}^{Con}$ and **(b)** $\Delta_{2,0}^{Geo}/M_{2,0}^{Con}$ around the shock wave front for different cases (explosion).

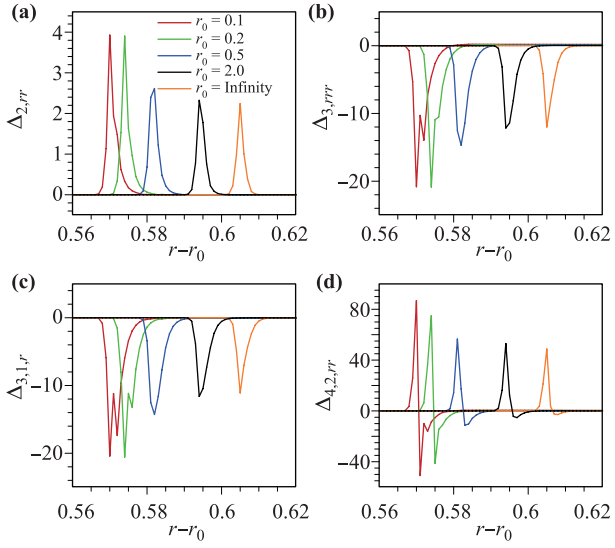

Fig. 14 The nonequilibrium quantities around wavefront for implosion.

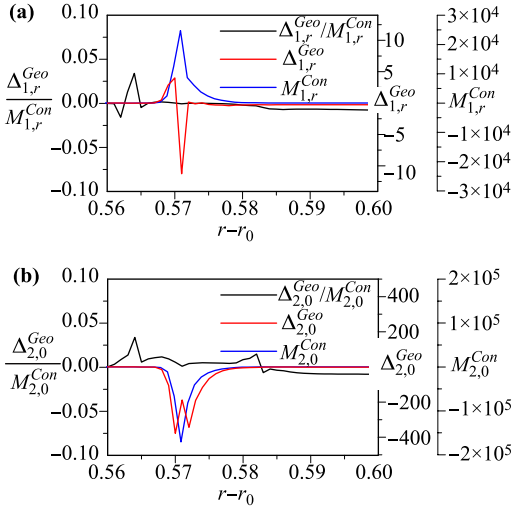

Fig. 15 The profiles of **(a)** $\Delta_{1,r}^{Geo}/M_{1,r}^{Con}$, $\Delta_{1,r}^{Geo}$, and $M_{1,r}^{Con}$ and **(b)** $\Delta_{2,0}^{Geo}/M_{2,0}^{Con}$, $\Delta_{2,0}^{Geo}$, and $M_{2,0}^{Con}$ around the shock wave front for the case with $r_0 = 0.1$ (implosion).

Comparisons between the error caused by the approximation $f \approx f^{eq}$ when calculating the "force term" and the convective term are given in Figs. 15 and 16. Profiles of $\Delta_{1,r}^{Geo}/M_{1,r}^{Con}$, $\Delta_{1,r}^{Geo}$, and $M_{1,r}^{Con}$ for the case with $r_0 = 0.1$ are shown in Fig. 15(a). It can be seen that $\Delta_{1,r}^{Geo}$ is so small compared with $M_{1,r}^{Con}$ that it nearly can be ignored even for such a small r_0. From Figure 15(b) we can see that $\Delta_{2,0}^{Geo}$ is also nearly negligible compared with $M_{2,0}^{Con}$. Besides, with the increase of r_0, the effects become weaker, with Δ_n^{Geo} becoming more negligible compared with M_n^{Con}, which is verified in Fig. 16.

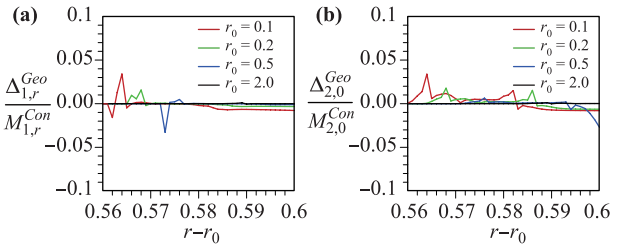

Fig. 16 The profiles of **(a)** $\Delta^{Geo}_{1,r}/M^{Con}_{1,r}$ and **(b)** $\Delta^{Geo}_{2,0}/M^{Con}_{2,0}$ around the shock wave front for different cases (implosion).

From Fig. 16 we can conclude that the error Δ^{Geo}_n is negligible compared with M^{Con}_n when $r_0 \geq 0.1$ for the current implosion numerical experiment setup.

4 Discussion and conclusion

We presented a theoretical framework for constructing a DBM in spherical coordinates for compressible flow systems with spherical symmetry. A key technique here is to use *local* Cartesian coordinates to describe the particle velocity. Thus, compared with the Boltzmann equation in Cartesian coordinates, geometric effects, such as divergence and convergence, are treated as a "force term." For such a system, even though the hydrodynamic model is one-dimensional, the DBM needs a discrete velocity model with three dimensions. A new scheme was introduced so that the DBM can use the same set of discrete velocities regardless of whether or not extra degrees of freedom are considered. We used 26 discrete velocities to formulate the DBM at the Navier–Stokes level.

Besides recovering the hydrodynamic equations in the continuum limit, two key points for a DBM were revealed: (i) In terms of nonconserved moments, we can define two sets of measures for the deviation of the system from its thermodynamic equilibrium state; (ii) in the regimes where the system deviates from its thermodynamic equilibrium, the DBM may present more reasonable density, flow velocity, and temperature than the corresponding Navier–Stokes model only if the second-order terms in the Knudsen number in the Chapman–Enskog expansion are taken into account in the model construction. With the DBM we can study *simultaneously* both hydrodynamic and thermodynamic behaviors. Because the inverse of the transformation matrix $\boldsymbol{C}$ connecting the discrete equilibrium distribution function $\boldsymbol{f}^{eq}$ and corresponding moments $\hat{\boldsymbol{f}}^{eq}$ has been fixed, the extension to multiple-relaxation-time DBMs [56] is straightforward. For the DBM in spherical coordinates, if we consider flow behavior near the spherical center, the "force term" (the term for geometric effects) should take into account the higher order nonequilibrium effects. Specifically, $f = f^{eq}$ should be replaced by $f = f^{eq} + f^{(1)}$, or even $f = f^{eq} + f^{(1)} + f^{(2)}$, etc. in the "force term". It should also be pointed out that fixing the transformation matrix $\boldsymbol{C}$ and its inverse is only one possible scheme to get a solution for the discrete equilibrium distribution function $\boldsymbol{f}^{eq}$. A second way to find a solution for the discrete equilibrium distribution function $\boldsymbol{f}^{eq}$ is to follow the ideas used in Ref. [52]. A difference is that the scheme introduced in this work needs a minimum number of discrete velocities.

Acknowledgements The authors would like to thank Drs. Chuandong Lin, Yanbiao Gan, and Feng Chen for helpful discussions. The work was supported by the National Natural Science Foundation of China [under Grant Nos. 11475028, 11772064, and U1530261] and the Science Challenge Project (under Grant Nos. JCKY2016212A501 and TZ2016002).

References

1. J. Buckmaster, T. L. Jackson, and A. Kumar, Combustion in High-Speed Flows, Springer Netherlands, 1994
2. L. F. Wang, W. H. Ye, X. T. He, J. F. Wu, Z. F. Fan, C. Xue, H. Y. Guo, W. Y. Miao, Y. T. Yuan, J. Q. Dong, G. Jia, J. Zhang, Y. J. Li, J. Liu, M. Wang, Y. K. Ding, and W. Y. Zhang, Theoretical and simulation research of hydrodynamic instabilities in inertial-confinement fusion implosions, *Sci. China Phys. Mech. Astron.* 60(5), 055201 (2017)
3. A. G. Xu, G. C. Zhang, Y. J. Ying, and C. Wang, Complex fields in heterogeneous materials under shock: modeling, simulation and analysis, *Sci. China Phys. Mech. Astron.* 59(5), 650501 (2016)
4. Z. H. Li and H. X. Zhang, Study on gas kinetic unified algorithm for flows from rarefied transition to continuum, *J. Comput. Phys.* 193(2), 708 (2004)
5. Z. H. Li, A. P. Peng, H. X. Zhang, and J. Y. Yang, Rarefied gas flow simulations using high-order gas-kinetic unified algorithms for Boltzmann model equations, *Prog. Aerosp. Sci.* 74, 81 (2015)
6. A. P. Peng, Z. H. Li, J. L. Wu, X. Y. Jiang, Validation and analysis of gas-kinetic unified algorithm for solving Boltzmann model equation with vibrational energy excitation, *Acta Physica Sinica* 66(20), 204703 (2017)
7. Z. H. Li, A. P. Peng, F. Fang, S. X. Li, and S. Y. Zhang, Gas-kinetic unified algorithm for hypersonic aerothermodynamics covering various flow regimes solving Boltzmann model equation, *Acta Physica Sinica* 64(22), 204703 (2015)
8. Z. Li, X. Jiang, J. Wu, A. Peng, Gas-kinetic unified algorithm for Boltzmann model equation in rotational nonequilibrium and its application to the whole range flow regimes, *Chin. J. Theor. Appl. Mech.* 46(3), 336 (2014)

9. W. Lei, J. M. Reese, and Y. Zhang, Solving the Boltzmann equation deterministically by the fast spectral method: Application to gas microflows, *J. Fluid Mech.* 746(746), 53 (2014)
10. L. Wu, J. Zhang, J. M. Reese, and Y. Zhang, A fast spectral method for the Boltzmann equation for monatomic gas mixtures, *J. Comput. Phys.* 298(C), 602 (2015)
11. J. Li, C. Zhong, Y. Wang, and C. Zhuo, Implementation of dual time-stepping strategy of the gas-kinetic scheme for unsteady flow simulations, *Phys. Rev. E* 95(5), 053307 (2017)
12. Y. Zhu, C. Zhong, and K. Xu, Implicit unified gas-kinetic scheme for steady state solutions in all flow regimes, *J. Comput. Phys.* 315, 16 (2016)
13. G. H. Tang, Y. H. Zhang, X. J. Gu, and D. R. Emerson, Lattice Boltzmann modelling Knudsen layer effect in non-equilibrium flows, *EPL* 83(4), 40008 (2008)
14. G. H. Tang, Y. H. Zhang, and D. R. Emerson, Lattice Boltzmann models for nonequilibrium gas flows, *Phys. Rev. E* 77(4), 046701 (2008)
15. G. H. Tang, X. J. Gu, R. W. Barber, D. R. Emerson, and Y. H. Zhang, Lattice Boltzmann simulation of nonequilibrium effects in oscillatory gas flow, *Phys. Rev. E* 78(2), 026706 (2008)
16. J. Meng, Y. Zhang, Kinetic diffuse boundary condition for high-order lattice Boltzmann model with streaming-collision mechanism, *J. Comput. Phys.* 258, 601 (2014)
17. J. Meng and Y. Zhang, Gauss-Hermite quadratures and accuracy of lattice Boltzmann models for nonequilibrium gas flows, *Phys. Rev. E* 83(3 Pt 2), 036704 (2011)
18. J. Meng, Y. Zhang, and X. Shan, Multiscale lattice Boltzmann approach to modeling gas flows, *Phys. Rev. E* 83(4 Pt 2), 046701 (2010)
19. J. P. Meng, N. Dongari, J. M. Reese, and Y. Zhang, A kinetic switching criterion for hybrid modelling of multiscale gas flows, *J. Phys. Confer. Ser.* 362(1), 12006 (2012)
20. J. Meng, Y. Zhang, N. G. Hadjiconstantinou, G. A. Radtke, and X. Shan, Lattice ellipsoidal statistical BGK model for thermal non-equilibrium flows, *J. Fluid Mech.* 718(3), 347 (2013)
21. K. Xu and J. C. Huang, A Unified Gas-Kinetic Scheme for Continuum and Rarefied Flows, Academic Press Professional, Inc., 2010
22. K. Xu and J. C. Huang, An improved unified gas-kinetic scheme and the study of shock structures, *IMA J. Appl. Math.* 76(5), 698 (2011)
23. J. C. Huang, K. Xu, and P. Yu, A unified gas-kinetic scheme for continuum and rarefied flows ii: multi-dimensional cases, *Commun. Comput. Phys.* 12(03), 662 (2012)
24. A. Xu, G. Zhang, and Y. Zhang, Discrete Boltzmann modeling of compressible flows, Chapter 2, in: Kinetic Theory, edited by G. Z. Kyzas and A. C. Mitropoulos, Croatia: InTech, 2018
25. A. G. Xu, G. C. Zhang, and Y. J. Ying, Progress of discrete Boltzmann modeling and simulation of combustion system, *Acta Physica Sinica* 64 64(18), 184701 (2015)
26. C. Lin, A. Xu, G. Zhang, Y. Li, and S. Succi, Polar-coordinate lattice Boltzmann modeling of compressible flows, *Phys. Rev. E* 89(1), 013307 (2014)
27. A. Xu, C. Lin, G. Zhang, and Y. Li, Multiple-relaxation-time lattice Boltzmann kinetic model for combustion, *Phys. Rev. E* 91(4), 043306 (2015)
28. Y. Gan, A. Xu, G. Zhang, and S. Succi, Discrete Boltzmann modeling of multiphase flows: Hydrodynamic and thermodynamic non-equilibrium effects, *Soft Matter* 11(26), 5336 (2015)
29. H. Lai, A. Xu, G. Zhang, Y. Gan, Y. Ying, and S. Succi, Nonequilibrium thermohydrodynamic effects on the Rayleigh-Taylor instability in compressible flows, *Phys. Rev. E* 94(2), 023106 (2016)
30. C. Lin, A. Xu, G. Zhang, and Y. Li, Double-distribution-function discrete Boltzmann model for combustion, *Combust. Flame* 164, 137 (2016)
31. Y. Zhang, A. Xu, G. Zhang, C. Zhu, and C. Lin, Kinetic modeling of detonation and effects of negative temperature coefficient, *Combust. Flame* 173, 483 (2016)
32. Y. Zhang, A. Xu, G. Zhang, and Z. Chen, Discrete Boltzmann method with Maxwell-type boundary condition for slip flow, *Commum. Theor. Phys.* 69(1), 77 (2018)
33. Y. Gan, A. Xu, G. Zhang, and H. Lai, Three-dimensional discrete Boltzmann models for compressible flows in and out of equilibrium, *Proc. Inst. Mech. Eng. C: J. Mech. Eng. Sci.* 232(3), 477 (2018)
34. C. Lin, A. Xu, G. Zhang, K. Luo, and Y. Li, Discrete Boltzmann modeling of Rayleigh-Taylor instability in bi-component compressible flows, *Phys. Rev. E* 96(5), 053305 (2017)
35. C. Lin, K. Luo, L. Fei, and S. Succi, A multi-component discrete Boltzmann model for nonequilibrium reactive flows, *Sci. Rep.* 7(1), 14580 (2017)
36. Y. Zhang, A. Xu, G. Zhang, Z. Chen, and P. Wang, Discrete ellipsoidal statistical BGK model and Burnett equations, *Front. Phys.* 13(3), 135101 (2018)
37. M. La Rocca, A. Montessori, P. Prestininzi, and S. Succi, A multispeed discrete Boltzmann model for transcritical 2d shallow water flows, *J. Comput. Phys.* 284(C), 117 (2015)
38. S. Succi, The Lattice Boltzmann Equation for Fluid Dynamics and Beyond, New York: Oxford University Press, 2001
39. S. Toppaladoddi, S. Succi, and J. S. Wettlaufer, Roughness as a route to the ultimate regime of thermal convection, *Phys. Rev. Lett.* 118(7), 074503 (2017)
40. X. Shan, X. Yuan, and H. Chen, Kinetic theory representation of hydrodynamics: A way beyond the Navier-Stokes equation, *J. Fluid Mech.* 550, 413 (2006)

41. J. Meng, Y. Zhang, N. G. Hadjiconstantinou, G. A. Radtke, and X. Shan, Lattice ellipsoidal statistical BGK model for thermal non-equilibrium flows, *J. Fluid Mech.* 718(3), 347 (2013)
42. D. Sun, M. Zhu, S. Pan, and D. Raabe, Lattice Boltzmann modeling of dendritic growth in a forced melt convection, *Acta Mater.* 57(6), 1755 (2009)
43. Y. Wang, C. Shu, H. B. Huang, and C. J. Teo, Multiphase lattice Boltzmann flux solver for incompressible multiphase flows with large density ratio, *J. Comput. Phys.* 280(C), 404 (2015)
44. Z. Chai, C. Huang, B. Shi, and Z. Guo, A comparative study on the lattice Boltzmann models for predicting effective diffusivity of porous media, *Int. J. Heat Mass Transfer* 98, 687 (2016)
45. H. Liu, L. Wu, Y. Ba, and G. Xi, A lattice Boltzmann method for axisymmetric thermocapillary flows, *International Journal of Heat & Mass Transfer* 104, 337 (2017)
46. L. Chen, L. Zhang, Q. Kang, H. S. Viswanathan, J. Yao, and W. Tao, Nanoscale simulation of shale transport properties using the lattice Boltzmann method: Permeability 445 and diffusivity, *Sci. Rep.* 5(1), 8089 (2015)
47. C. Zhuo, C. Zhong, and J. Cao, Filter-matrix lattice Boltzmann model for incompressible thermal flows, *Phys. Rev. E* 85(4), 046703 (2012)
48. J. Meng and Y. Zhang, Diffuse reflection boundary condition for high-order lattice Boltzmann models with streaming-collision mechanism, *J. Comput. Phys.* 258(C), 601 (2014)
49. L. Wang, G. Zhou, X. Wang, Q. Xiong, and W. Ge, Direct numerical simulation of particle-fluid systems by combining time-driven hard-sphere model and lattice Boltzmann method, *Particuology* 8(4), 379 (2010)
50. A. Doostmohammadi, T. N. Shendruk, K. Thijssen, and J. M. Yeomans, Onset of meso-scale turbulence in active nematics, *Nat. Commun.* 8, 15326 (2017)
51. A. G. Xu, G. C. Zhang, Y. B. Gan, F. Chen, and X. J. Yu, Lattice Boltzmann modeling and simulation of compressible flows, *Front. Phys.* 7(5), 582 (2012)
52. M. Watari and M. Tsutahara, Possibility of constructing a multispeed Bhatnagar–Gross–Krook thermal model of the lattice Boltzmann method, *Phys. Rev. E* 70(1), 016703 (2004)
53. H. Liu, W. Kang, Q. Zhang, Y. Zhang, H. Duan, and X. T. He, Molecular dynamics simulations of microscopic structure of ultra strong shock waves in dense helium, *Front. Phys.* 11(6), 115206 (2016)
54. H. Liu, Y. Zhang, W. Kang, P. Zhang, H. Duan, and X. T. He, Molecular dynamics simulation of strong shock waves propagating in dense deuterium, taking into consideration effects of excited electrons, *Phys. Rev. E* 95, 023201 (2017)
55. H. Liu, W. Kang, H. Duan, P. Zhang, and X. He, Recent progresses on numerical investigations of microscopic structure of strong shock waves in fluid, *Scientia Sinica Physica Mechanica and Astronomica* 47(7), 070003 (2017)
56. F. Chen, A. G. Xu, G. C. Zhang, and Y. L. Wang, Two-dimensional MRT LB model for compressible and incompressible flows, *Front. Phys.* 9(2), 246 (2014)